

# **A weakly-supervised deep learning model for fast localisation and delineation of the skeleton, internal organs, and spinal canal on Whole-Body Diffusion-Weighted MRI (WB-DWI)**

*Antonio Candito<sup>1</sup>, Alina Dragan<sup>1,2</sup>, Richard Holbrey<sup>1</sup>, Ana Ribeiro<sup>2</sup>, Ricardo Donners<sup>3</sup>, Christina Messiou<sup>1,2</sup>, Nina Tunariu<sup>1,2</sup>, Dow-Mu Koh<sup>1,2</sup>, and Matthew D Blackledge<sup>1</sup>*

<sup>1</sup>The Institute of Cancer Research, London, United Kingdom

<sup>2</sup>The Royal Marsden NHS Foundation Trust, London, United Kingdom

<sup>3</sup>University Hospital Basel, Basel, Switzerland

Corresponding Author: Matthew D Blackledge  
The Institute of Cancer Research, London (UK)  
Matthew.Blackledge@icr.ac.uk

**Keywords:** Deep learning; Segmentation; Whole-Body Diffusion-Weighted MRI (WB-DWI); Quantitative Imaging Biomarkers; Metastatic bone disease; Multiple Myeloma

## **Abstract:**

**Background:** Apparent Diffusion Coefficient (ADC) values and Total Diffusion Volume (TDV) from Whole-body diffusion-weighted MRI (WB-DWI) are recognised cancer imaging biomarkers. However, manual disease delineation for ADC and TDV measurements is unfeasible in clinical practice, demanding automation. As a first step, we propose an algorithm to generate fast and reproducible probability maps of the skeleton, adjacent internal organs (liver, spleen, urinary bladder, and kidneys), and spinal canal.

**Methods:** We developed an automated deep-learning pipeline based on a 3D patch-based Residual U-Net architecture that localises and delineates these anatomical structures on WB-DWI. The algorithm was trained using “soft-labels” (non-binary segmentations) derived from a computationally intensive atlas-based approach. For training and validation, we employed a multi-centre WB-DWI dataset comprising 532 scans from patients with Advanced Prostate Cancer (APC) or Multiple Myeloma (MM), with testing on 45 patients.

**Results:** Our weakly-supervised deep learning model achieved an average dice score/precision/recall of 0.66/0.6/0.73 for skeletal delineations, 0.8/0.79/0.81 for internal organs, and 0.85/0.79/0.94 for spinal canal, with surface distances consistently below 3mm. Relative median ADC and log-transformed volume differences between automated and manual expert-defined full-body delineations were below 10% and 4%, respectively. The computational time for generating probability maps was 12x faster than the atlas-based registration algorithm (25sec vs. 5min). An experienced radiologist rated the model's accuracy "good" or "excellent" on tests datasets.

**Conclusion:** Our model offers fast and reproducible probability maps for localising and delineating body regions on WB-DWI, enabling ADC and TDV quantification, potentially supporting clinicians in disease staging and treatment response assessment.

## **1. Background**

Whole-body diffusion-weighted MRI (WB-DWI) allows for the identification, staging, and response assessment of systemic malignant disease in patients diagnosed with Advanced Prostate Cancer (APC) or Multiple Myeloma (MM) [1]–[3]. This non-invasive and radiation-free imaging modality detects malignant lesions by visualising and quantifying differences in water mobility between healthy and cancerous regions [4]. Bone lesions exhibit high DWI signal intensity due to restricted water mobility within tumour-infiltrated bone marrow [5]. Moreover, the use of short-tau inversion recovery (STIR) fat suppression eliminates signal from yellow marrow, further enhancing lesion contrast from normal bone marrow background in the older population [6]. The mobility of water may be quantified by calculating the Apparent Diffusion Coefficient (ADC) from studies that acquire images at 2 or more b-values (typically 0-50 and 900-1000 s/mm<sup>2</sup>). This marker was shown to inversely correlate with tissue cellularity and can be used as a potent biomarker of response [7], [8]. Furthermore, the Total Diffusion Volume (TDV, in millilitres) of delineated bone disease in WB-DWI may be used to reflect the estimated tumour burden [9], [10]. These quantitative imaging biomarkers are clinically validated and have been included in radiological guidelines for reporting metastatic bone disease (METastasis Reporting and Data System for Prostate Cancer, MET-RADS-P [11]) and MM patients (Myeloma Response Assessment and Diagnosis System, MY-RADS [12]).

However, radiologists need to manually delineate bone lesions throughout the patient's skeleton to measure ADC and TDV. This process is cumbersome and time-consuming, often requiring an hour or more, depending on disease burden [13]. As a result, manual delineation is not feasible for routine reporting workflows. There is a growing clinical demand for software solutions that can automate this task, assisting radiologists in quantifying bone disease in patients diagnosed with APC or MM [14]. We hypothesise that a logical first step toward automation is developing an algorithm to localise and delineate the whole skeleton along with adjacent internal organs (urinary bladder, kidneys, liver, and spleen) and the spinal canal contents (spinal cord and surrounding CSF) from WB-DWI scans. This

would isolate bone from adjacent anatomical structures and/or non-skeletal regions that exhibit hyperintense signals on b900 images.

Recent studies in MM patients have investigated histogram analysis parameters of total tumour ADC and their correlation with treatment response [15]. Wang et al. [16] extended this approach to background bone marrow (avoiding focal lesions) and found it to be a sensitive predictor of high-risk disease in multiple-myeloma (R-ISS stage III). There is consequently potential benefit in extending the delineation and ADC histogram analysis to the entire skeleton, rather than limiting it to the tumour volume. Furthermore, histogram analysis might not be feasible in the post-treatment setting if the delineation is limited to active disease only, as some patients undergo very good or complete response to treatment, leaving a limited amount or no active disease for post treatment delineation. This limitation could be overcome if the bone marrow space is automatically delineated and analysed as a whole.

Atlas-based registration algorithms have been proposed for automatic delineation of the skeleton and internal organs from higher resolution and higher SNR images, including CT scans, T1-weighted (T1w), and T2-weighted (T2w) MRI [17]–[19]. However, the accuracy of these delineations may be affected by the characteristics of the atlas cohort, including the extent of disease spread across patients and how experts defined the ground truth, as well as the initial spatial alignment between whole-body target and atlas image [20], [21]. Also, the computational time required for registrations may hinder clinical deployment.

Supervised deep learning models offer the potential to improve performance over atlas-based registration algorithms for delineation tasks from medical images [22]–[24]. Several studies have introduced different model architectures to accurately delineate multi-organs from whole-body CT scans, T1w, and T2w MRI [25]–[29]. For example, the “*TotalSegmentator-CT*” [30], trained on a large (1024 patients), multi-centre, and multi-vendor CT dataset, has shown the ability to delineate 117 body regions with excellent agreement to manual delineations on external test datasets. However, the development of such models requires fully annotated images [31], which are challenging to obtain for

WB-DWI. Despite these advancements in deep learning-based algorithms for organ delineation from whole-body medical imaging, automated delineation of the bone marrow space from WB-DWI scans remains a complex task due to inter-patient heterogeneity, the varied appearance and distribution of disease, and the presence of imaging artifacts due to low SNR or magnetic susceptibility effects.

In this article, we present the development of an automated deep learning pipeline for deriving annotations of skeletal regions (legs, pelvis, lumbar/thoracic/cervical spine, ribcage, and arms/shoulders), along with adjacent internal organs (liver, spleen, urinary bladder, and kidneys) and the spinal canal contents (spinal cord and CSF) from b-value images and ADC maps. We use a weakly-supervised approach where “soft-labels” (non-binary segmentations) derived from a previously described atlas-based segmentation method, which generates a voxel-wise probability of each voxel belonging to a specific region. Although these labels are less precise than manual annotations, they enable the training of a significantly faster weakly-supervised deep learning model that leverages an extensive multi-centre dataset of WB-DWI scans from patients diagnosed and treated for APC or MM. As a result, the trained model can quickly generate reproducible probability maps for localising and delineating body regions from WB-DWI.

Our innovative weakly-supervised deep learning model could address the limitations of existing algorithms by: (i) reducing registration errors caused by initial spatial alignment between target and atlas images, (ii) decreasing the computational time required for whole-body registration, (iii) eliminating the need for time-consuming manual annotations by radiologists during model development, (iv) offering soft-boundaries maps that capture anatomical structures with unclear boundaries due to disease spread, and the low resolution and geometric distortion of DWI.

## **2. Methods**

### **2.1 Patient Population**

To train the weakly-supervised deep learning model, we used three anonymised and retrospective WB-DWI datasets. **Dataset A** consisted of 217 patients diagnosed with APC, and **Dataset B** comprised 127 patients with confirmed MM (**Table 1**). These datasets were obtained from three different imaging centres, each varying in experience with WB-DWI protocols for oncological investigations. Finally, **Dataset C** consisted of 15 patients (13 male, 2 female) with confirmed MM with diffuse pattern disease, with images captured at a single centre. These images were manually contoured and defined our cohort for atlas-based segmentation.

In **Dataset A**, each patient underwent both pre- and post-treatment scanning, typically performed three months after treatment initiation to assess response or disease progression. These scans were acquired at one of three imaging centres, with 188, 22, and 7 patients per centre, respectively. For patients with confirmed MM (**Dataset B**), baseline scans were obtained at one of two imaging centres, with 113 and 14 patients per centre. Additionally, 12.6% of MM patients had a post-treatment scan, which was included in the dataset alongside the baseline scans from all patients. The total number of scans from male and female patients was 497 and 80, respectively. Patients from each dataset were divided into training, validation, and test cohorts. Two experienced radiologists [*NT and CM blinded for review*] in functional cancer imaging and WB-DWI selected 15 patients with APC and 15 patients with MM from **Datasets A and B**, respectively, for the test cohort. The remaining patients (314) were split (80:20) into training and validation cohorts, resulting in 251/425 patients/scans for the training set and 63/107 patients/scans for the validation set.

All data were fully anonymised, and the study was performed following the Declaration of Helsinki (2013). A local ethical committee waived the requirement of patient consent for the use of these retrospective datasets.

## 2.2 Whole-body MRI protocol

WB-DWI scans were acquired between 2015 and 2023 using two (50/900 s/mm<sup>2</sup>) or three (50/600/900 s/mm<sup>2</sup>) b-value diffusion weighted images on a 1.5T scanner (MAGNETOM Aera/Avanto, Siemens Healthcare, Erlangen, Germany). The scans covered 5-7 stations from the skull base to mid-thigh (for APC) or from the skull vertex to the knees (for MM). Each station consisted of 40 slices with a slice thickness of 5-6 mm. DWI was acquired as axial 2D single shot echo-planar imaging with acceleration factor 2 (GRAPPA) and three/four scan trace encoding directions. Additionally, STIR fat suppression with an inversion time of 180ms was employed to enhance image quality and contrast. All MRI parameters for DWI sequence are reported in **Table 1** for each dataset involved in the study. The whole-body MRI protocol also provides complementary morphological and functional imaging through the acquisition of sagittal T1/T2 spine images and 3D T1w DIXON images [32]. This is a valid and widely accepted protocol, included in radiological guidelines and recommendations for reporting metastatic bone disease (MET-RADS-P [11]) and patients diagnosed with MM (MY-RADS-P [12]).

**Table 1.** Scanning protocol and MRI parameters for all WB-DWI datasets investigated in our study. Minimum and maximum values are displayed in parenthesis.

	APC - Dataset (A) (217 patients, 434 WB-DWI scans)		MM - Dataset (B) (127 patients, 143 WB-DWI scans)		MM Atlas - Dataset (C) (15 patients, 15 WB-DWI scans)	
<b>Dataset Split</b>	Training: 160 patients, 320 scans  Validation: 42 patients, 84 scans  Test: 15 patients, 30 scans		Training: 91 patients, 105 scans  Validation: 21 patients, 23 scans  Test: 15 patients, 15 scans		Leave-one-out cross-validation (LOOCV) for registration algorithm,  Test dataset for deep-learning models	
<b>MR scanner</b>	1.5T Siemens Aera		1.5T Siemens Aera		1.5T Siemens Aera	
<b>Sequence</b>	Diffusion-Weighted SS-EPI		Diffusion-Weighted SS-EPI		Diffusion-Weighted SS-EPI	
<b>Acquisition plane</b>	Axial		Axial		Axial	
<b>Breathing mode</b>	Free breathing		Free breathing		Free breathing	
<b>b-values [s/mm<sup>2</sup>]</b>	b50/b900 (N = 21)	b50/b600/b900 (N = 196)	b50/b900 (N = 25)	b50/b600/b900 (N = 102)	b50/b900 (N = 6)	b50/b600/b900 (N = 9)
<b>Number of averages per b-value</b>	(3,5)	[(2,2,4) - (3,6,6)]	(4,4)	(2,2,4)	(4,4)	(3,3,3)
<b>Reconstructed resolution [mm<sup>2</sup>]</b>	[1.56x1.56 - 3.12x3.12]		[1.54x1.54 - 1.68x1.68]		[1.54x1.54 - 1.68x1.68]	
<b>Slice thickness [mm]</b>	[5 - 6]		5		5	
<b>Repetition time [ms]</b>	[5490 - 12700]		[6150 - 14500]		[6150 - 14500]	
<b>Echo time [ms]</b>	[60 - 79]		[66.4 - 69.6]		[64 - 69.9]	
<b>Inversion time (STIR fat suppression) [ms]</b>	180		180		180	
<b>Flip angle [°]</b>	90		90		90	
<b>Reconstructed matrix [mm]</b>	[98x128 - 256x256]		[208x256 - 224x280]		[208x256 - 224x280]	
<b>Receive bandwidth [Hz/Px]</b>	[1955 - 2330]		[1984 - 2330]		[1953 - 2330]	



## 2.3 AI-model for body regions localisation and delineation

An overview of the proposed pipeline for our weakly-supervised deep learning model is illustrated in **Figure 1**.

### 2.3.1 Soft-label annotation using atlas-based registration

To generate soft-labels for deep-learning model training, we employed a previously described atlas-based technique [33]. For all patients in our atlas cohort (**Dataset C**), a consultant radiologist [*AD blinded for review*] with 5+ years of experience in functional cancer imaging, manually delineated the whole skeleton and internal organs on the DWI sequence across all 15 scans. They assigned labels to seven different skeletal regions (legs, pelvis, lumbar/thoracic/cervical spine, ribcage, and arms/shoulders) and four internal organs (liver, spleen, urinary bladder, and kidneys). This cohort only included MM patients with diffuse disease for the following reasons: (i) MM scans have generally the widest coverage (from skull vertex to knees) within our centre, and (ii) patients diagnosed with diffuse disease pattern exhibits elevated skeleton diffusion signal allowing the bone to be more easily identified.

For segmentation of each new patient in the training/validation cohort of **Datasets A and B** (“target data”), we firstly registered the calculated ADC maps from each of the fifteen delineated patients in the atlas cohort (“atlas data”). Two AI-based models were employed for optimising the initial alignment between the atlas and target data, as previously described [33], [34]: (i) a body region classifier that automatically predicts the position of axial images into one of six potential body regions (legs, pelvis, lumbar/thoracic/cervical spine, and head), and (ii) a model that automatically delineates the spinal cord and surrounding CSF using a trained 2D U-Net model. After applying this initial alignment, registration was fine-tuned using affine followed by non-linear diffeomorphic demons transformation [35]. We utilised a mean squared error (MSE) optimisation between the target and atlas ADC data. For affine registration, we employed an Amoeba optimiser (simplex delta = 0.005) with shrink factors (4, 2, 1), smoothing sigmas (4, 2, 0), and a maximum of 200 iterations. For deformable demons registration, Gradient Descent optimisation was applied (learning rate = 2) with non-rigid shrink factors (4, 2, 1),

smoothing widths (4, 2, 0), and a convergence window size of 20. The convergence tolerance for both methods was set to  $10^{-6}$ .

The derived transforms were then applied to all the pre-counteracted body region masks in the atlas cohort. Transformed masks from the same region were combined using a weighted summation, where the weights are the reciprocal of the MSE values:

$$P_j = \frac{\sum_{i=1}^{15} \frac{1}{MSE_i} \cdot T_i(M_{ij})}{\sum_{i=1}^{15} \frac{1}{MSE_i}} \quad (3)$$

Where:

- $P_j$  is a probability for each voxel that the voxel belongs to tissue class  $j$ .
- $T_i$  is the registration transform derived for atlas patient  $i$ .
- $M_{ij}$  denotes the (untransformed) mask for tissue class  $j$  in each atlas patient  $i$ .
- $MSE_i$  is the mean squared error in ADC values between atlas patient  $i$  and the target new patient following registration.

The labels for the spinal cord and surrounding CSF were directly derived from the 2D U-Net model, resulting in 12 probability maps, as illustrated in **Figure 1**. Probability maps were stacked to generate the soft-labels in tensor form, each including 13 channels per WB-DWI scan, where the last channel was dedicated to representing the image background:  $P_{background} = 1 - \sum_{j=1}^{12} P_j$ , which is guaranteed to remain between 0 and 1.

### 2.3.2 Weakly-supervised model training

A 3D patch-based Residual U-Net model (Res U-Net) [36] was trained to generate skeleton, internal organ, and spinal canal probability maps, using soft-labels obtained from the soft-label annotation phase. The networks involved a 2-channel input: (i) the ADC map (no thresholding was applied to remove negative ADC calculations) and (ii) the estimated intercept (S0) image at  $b = 0$  s/mm<sup>2</sup>. The ADC map and S0 image were derived by fitting a monoexponentially decaying model to the diffusion data included in the training and validation cohorts [37], [38]. The multi-channel, SoftMax output of

the model was the probability maps of seven skeleton regions, four internal organs, spinal canal, and in the last channel the image background. All images in the training and validation cohorts were interpolated to matrix = 256 x 256 and resolution = 1.6 x 1.6 mm. Input images were normalised using the following transformations:

$$\textit{scaled ADC map} = \textit{ADC map} / 3.5 \cdot 10^{-3} \textit{ mm}^2/\textit{s} \quad (4)$$

$$\textit{scaled S0 image} = \log(\textit{S0 image}) / \max(\log(\textit{S0 image})) \quad (5)$$

The Res U-Net symmetrical encoder-decoder architecture consisted of 5 convolutional layers, with the number of filters down-sampled or up-sampled by a factor of 2 at each layer, starting from 32 filters. Each layer employed skip connections between corresponding encoder and decoder paths. All convolutional layers used a 3x3 kernel size with a stride of 2, batch normalisation, a dropout rate of 0.2, and the ReLU activation function, except for the final output layer, which used a SoftMax activation function. Residual connections were implemented in each layer of the encoder and decoder paths to mitigate the vanishing gradient problem. We employed stochastic gradient descent optimization with hyperparameters: learning rate of 0.1, momentum of 0.9, and weight decay of  $4 \cdot 10^{-5}$ , aimed at minimizing a multi-class cross-entropy loss function. The training process lasted 300 epochs, using a batch size of 4 and patch size of 128x128x64. Our choice of batch and patch sizes aimed to enhance memory efficiency, mitigate overfitting, and improve generalisation capabilities, all while maintaining focus on the local details critical for accurate delineation in medical images [39]. All algorithms were implemented in Python (v.3.7) using PyTorch v.1.12.1 and MONAI v.0.9.1 toolboxes, running upon a Windows platform (v.10.0.19) accelerated by an NVIDIA RTX6000 GPU (Santa Clara, California, US). After training, the weakly-supervised Res U-Net model can automatically generate probability maps for body regions from a new WB-DWI scan using pre-processed ADC maps and S0 images, eliminating the need for computing atlas-based registration algorithms.

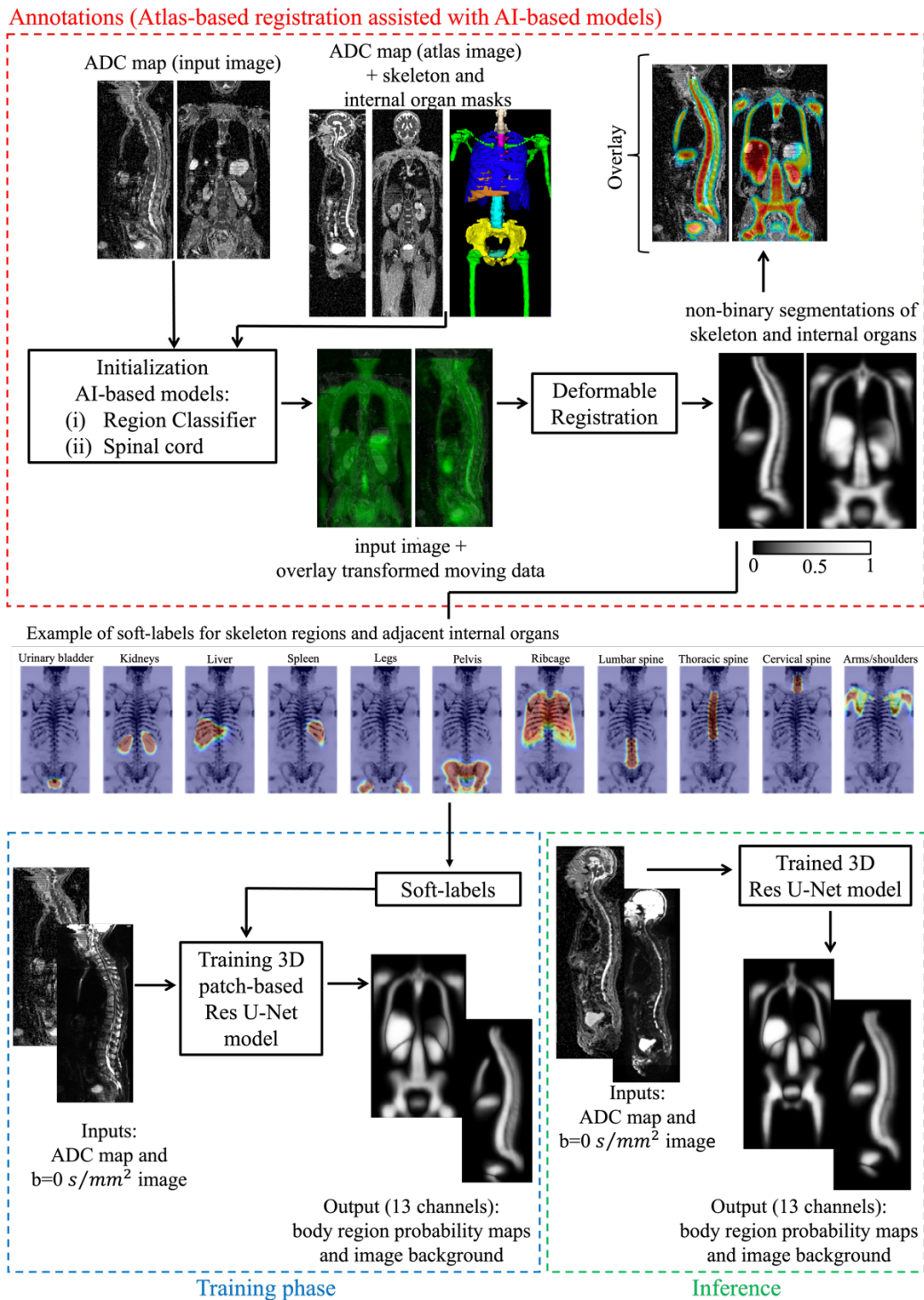


**Figure 1.** Automated end-to-end pipeline for developing a weakly-supervised deep learning model that automatically localises/delineates seven skeleton regions (legs, pelvis, ribcage, lumbar/thoracic/cervical spine, and arms/shoulders), four adjacent internal organs (liver, spleen, urinary bladder, and kidneys) and the spinal canal from WB-DWI scans. We employed an atlas-based registration assisted with two previously trained AI-based models for generating soft-labels (non-binary segmentations). Next, we used the soft-labels for training a faster 3D patch-based Res U-Net model with 2-channel input, the ADC map and  $b = 0 \text{ s/mm}^2$  image, and as output (13 channels) the body region probability maps alongside the image background. As a result, for a new input WB-DWI, the trained Res U-Net model can generate all body region probability maps without any registration step.

## 2.4 Evaluation Criteria

### 2.4.1 Quantitative analysis

We compared the accuracy of our deep-learning model to expert annotations within the atlas patient cohort (**Dataset C**). This might be seen as a potential weakness, however, the ADC maps and S0 images from the atlas dataset were not used directly for training. Therefore, we argue that the results would form a valid test of our model’s performance. To compare our approach with that of conventional atlas-based segmentation, we employed a leave-one-out-cross-validation (LOOCV) strategy. For each of the 15 patients, we derived (i) an atlas-based segmentation using the method described in section 2.3.1 using the remaining 14 patients, and (ii) a segmentation as estimated using our proposed deep-learning model. In each case we calculated the dice similarity coefficient (DSC), precision, recall, and average surface distance for all body regions based on both derived and manual segmentations. We also transferred the automated and manual body region masks onto the ADC map to calculate ADC statistics (median) and body region volumes (log-transformed), reporting the relative differences. Significant differences between the results derived from both automated methods were assessed using a Wilcoxon signed-rank test ( $p < 0.05$  indicating significance), with the best method selected based on the highest DSC and the lowest computational time.

### 2.4.2 Probability Calibration

Probabilities generated by machine learning models must be calibrated so that outputs reflect true likelihoods [40]. We calibrated the output of our deep learning model using all patients in **Datasets C**: each channel of the SoftMax output of our model was partitioned into 20 equidistant intervals,  $x$ , with boundaries  $[0, 0.05, \dots, 0.95, 1]$ ; for pixels that fell within each partition we then calculated the proportion occupied with that ground-truth label,  $y$ , from manual delineation. The generated curves then indicate whether the model output under- or over-estimates true label frequencies during segmentation and thus represents a valid probability distribution [41].

We used isotonic regression to calibrate the model outputs, which ensures a monotonic relationship between the predictor and target variables [42]. This technique is formulated as an optimisation problem, expressed as:

$$\min \sum_{i=1}^n (y_i - f(x_i))^2 \text{ subject to } f(x_1) \leq f(x_2) \dots \leq f(x_n) \quad (6)$$

For our multi-class model, we employed a one-vs-all strategy [43]. Each channel was calibrated in turn, with the remaining channels being grouped together as the negative class. The success of the weakly-supervised model calibration was evaluated by calculating the log-loss between the true labels and calibrated probability maps derived from the isotonic regression fitting. A decrease in the log-loss indicates the success of the calibration process, ensuring true probabilities and mitigating under- and over-predictions by the trained Res U-Net model.

### 2.4.3 Semi-quantitative analysis

A consultant radiologist [*AD blinded for review*] completed a semi-quantitative analysis to evaluate the accuracy of our segmentation model in our 30 test-patient cohort (15 APC and 15 MM). They assessed segmentation quality by superimposing estimated probability maps for all body regions onto the ADC maps and high b-value images ( $b = 900 \text{ s/mm}^2$ ). A qualitative assessment was made using a 4-point Likert scale: 1 = segmentation failure, 2 = suboptimal performance, 3 = good accuracy, and 4 = excellent accuracy. Criteria considered for each WB-DWI scan assessment were: (i) the degree to which the location of the body region probability maps matched the actual patient anatomy, further verified by reviewing T1/T2 spine and whole-body DIXON T1w images; (ii) the success of the derived delineations in covering the volume of the skeleton and internal organs visible on the WB-DWI scan; (iii) how well the automated delineations separated different anatomical structures (e.g., ensuring predicted kidney masks did not overlap with actual liver boundaries). Finally, this expert assessment would provide insights into whether the automated tool is sufficiently developed to serve as preliminary step in isolating the whole bone marrow background, facilitating the development of signal-based AI tools for automated bone lesion detection/delineation from WB-DWI scans.

### **3. Results**

#### **3.1 Calibration**

In **Figure 2**, we demonstrated the reliability curves for each body region in **Dataset C**. These curves revealed that the weakly-supervised Res U-Net model tended to overestimate or underestimate predictions compared to the true probabilities. In the uncalibrated models for binary classification, data points consistently fell below or above the ideal calibration line. However, following calibration using the isotonic regression technique, we observed a notable decrease in log-loss (on average -15%) compared to the uncalibrated models, with data points moving closer to the ideal calibration line.

#### **3.2 Quantitative analysis**

**Figure 3** shows the overlap-based metrics alongside relative median ADC and volume differences from both manual and automated masks following calibration for each body region. The weakly-supervised Res U-Net model outperformed the atlas-based registration algorithm, with average DSC values for all body regions increasing by more than 8%, demonstrating statistically significant differences between the methods. The computational time required to generate probability maps from the model averaged 25 seconds, compared to the 5 minutes needed for the atlas-based registration algorithm on the same hardware (2.4 GHz Quad-Core Intel Core i5).

Our weakly-supervised deep learning model achieved the following results for skeleton delineations: a DSC, precision, and recall of 0.66/0.6/0.73, with an average surface distance between automated and manual expert-defined delineations of less than 2mm. Significant improvements compared to the atlas-based registration algorithm were observed in the pelvis, lumbar, and thoracic spine regions, where we obtained a DSC, precision, and recall of 0.75/0.73/0.78. For long bones and the cervical spine, these overlap-based metrics were slightly lower, averaging just below 0.7. However, performance decreased for the ribcage, with a DSC of 0.47, precision of 0.38, and recall of 0.62. In terms of internal organs, our model achieved a DSC, precision, and recall of 0.8/0.79/0.81. The spleen yielded the lowest score among soft tissues, with an average surface distance exceeding 3mm. We observed a statistically

significant reduction in relative median ADC and volume differences for whole skeleton delineations compared to the atlas-based registration algorithm. The relative median ADC differences for the skeleton and internal organs between automated and manual expert-defined delineations were below 11% and 4%, respectively, except for the bladder, which exceeded 14%. The relative log-transformed volume differences between manual and automated methods for skeleton and internal organs remained below 2%, except for the ribcage, bladder, and spleen, which surpassed 5%. Spinal canal delineations showed a DSC of 0.85, precision of 0.79, and recall of 0.94, consistent with results from the 2D U-Net model. **Figures 4 and 5** present manual and derived delineations of the skeleton, internal organs, and spinal canal for three randomly selected test cases (**Dataset C**), confirming the weakly supervised deep learning model's ability to localise and delineate body regions from WB-DWI scans.



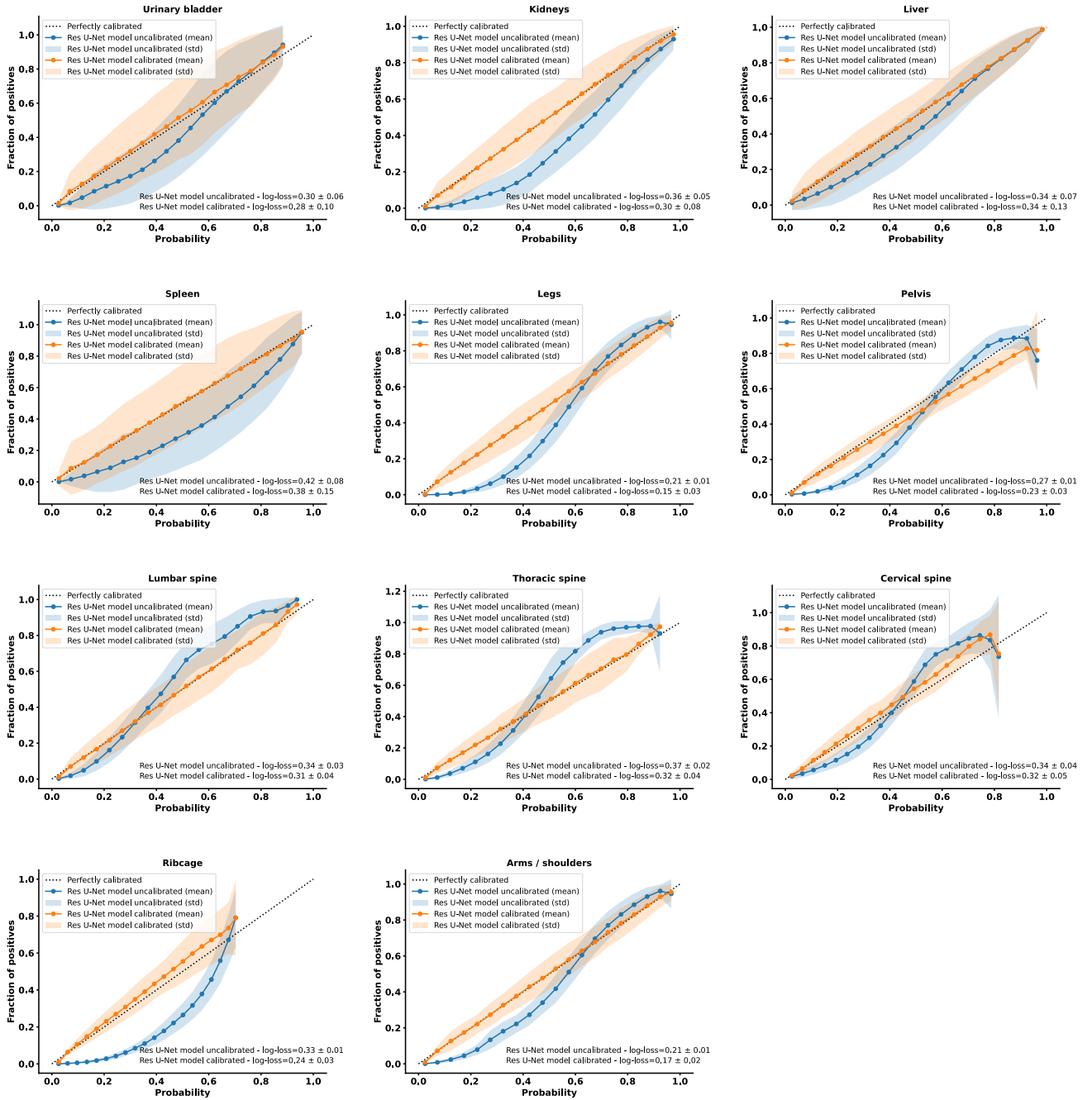


**Figure 2.** Reliability curves used to evaluate the calibration of the weakly-supervised Res U-Net model. To perform this analysis, we used all patients included in the atlas cohort (**Dataset C**), with a leave-one-out testing approach. Confidence intervals (mean and standard deviation) were calculated for each data point in the plots. We generated 11 reliability curves, assuming models trained for a binary classification task (one-vs-all strategy). Importantly, predictions (all voxels) from the SoftMax activation function (uncalibrated model) tended to overestimate or underestimate true probabilities, as evidenced by data points falling below or above the  $y=x$  line. In contrast, models calibrated using the isotonic regression technique demonstrated a reduced log-loss between true labels and predicted probabilities, with data points aligning closer to the ideal calibration curves. This calibration process ensures that model predictions accurately reflect true probabilities, thereby mitigating the risks associated with under or over predictions.

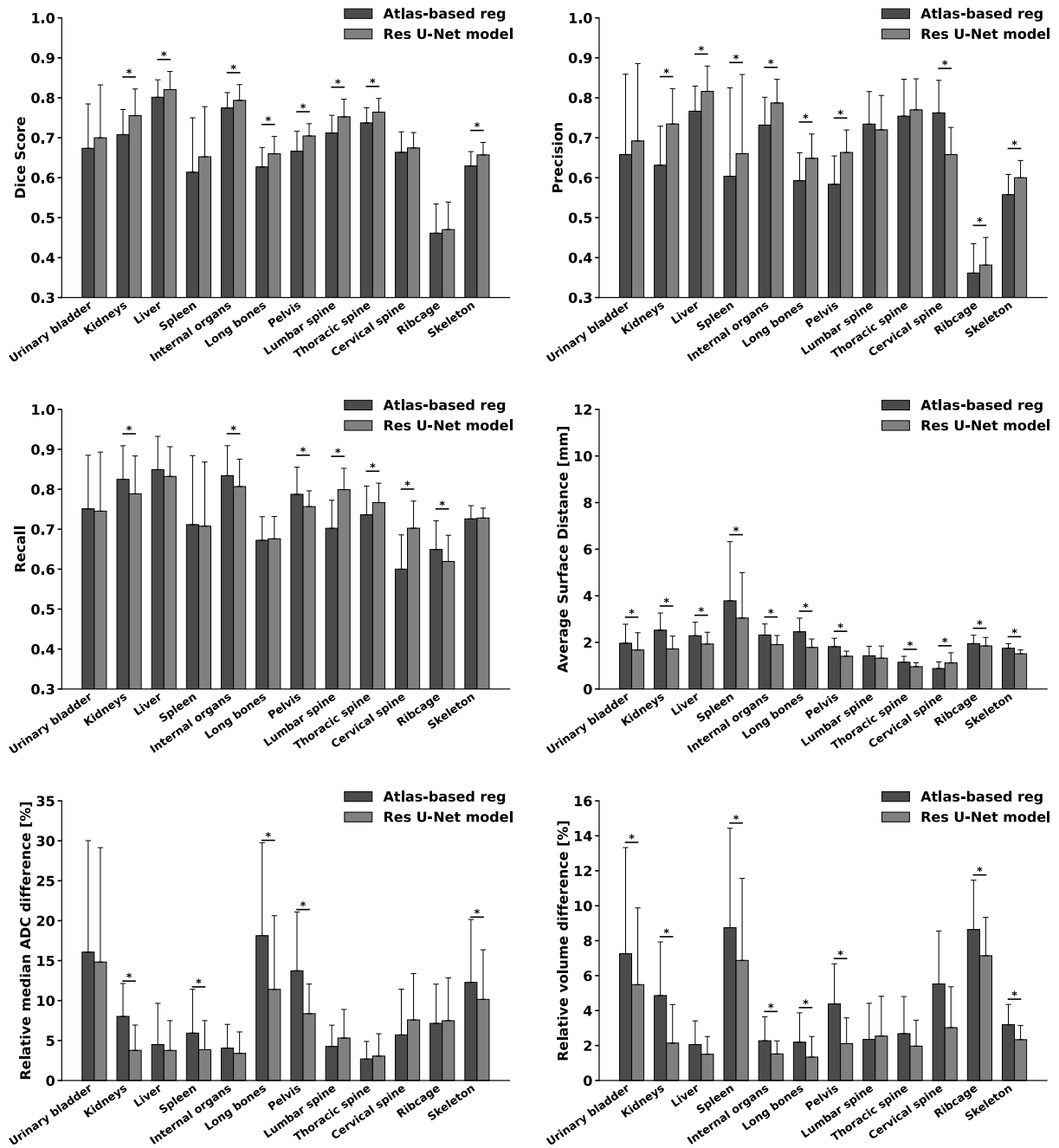


**Figure 3.** Quantitative metrics for evaluating the performance of the calibrated weakly-supervised 3D Res U-Net model in localising and delineating body regions from WB-DWI scans (**Dataset C**), compared to expert-defined delineations. Additionally, the same metrics were derived using the atlas-based registration algorithm (baseline) through LOOCV. Overlap-based metrics showed a significant improvement for the deep-learning model over the registration algorithm across all body regions, with at least an 8% increase in DSC. Moreover, the model generated outputs 12 times faster than the registration algorithm (25 seconds versus 5 minutes). Our weakly-supervised model also showed lower relative median ADC and log-transformed volume differences, with statistically significant differences observed for whole skeleton delineations. Mask for long bones consisted of legs and arms/shoulders. Mask for skeleton included long bones, pelvis, lumbar/thoracic/cervical spine, and ribcage. Mask for internal organs included urinary bladder, kidneys, liver and spleen.

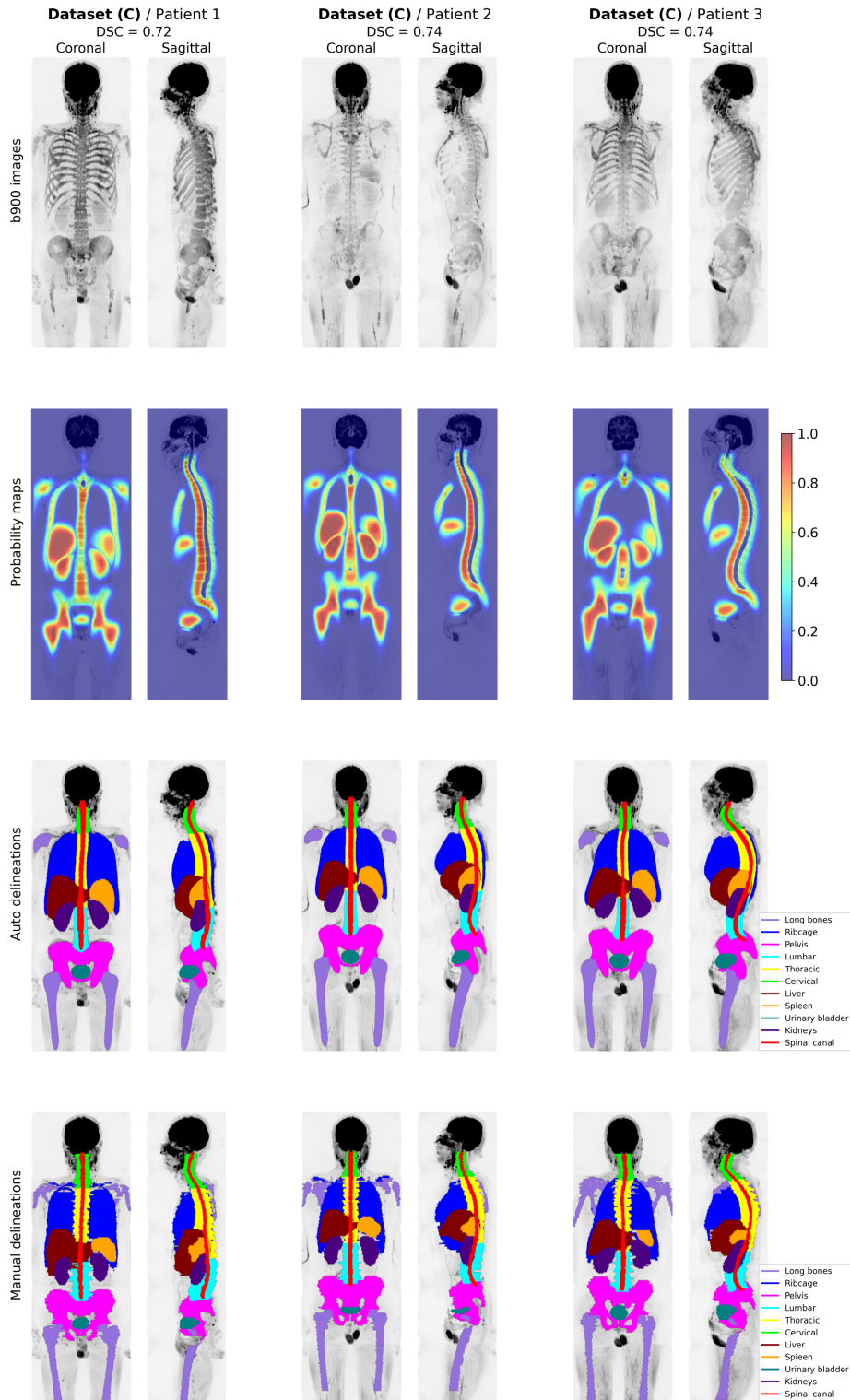


**Figure 4.** Sagittal and coronal views of Maximum Intensity Projection (MIP) of b900 images for three randomly selected test cases from **Dataset C** (top row). The second to fourth rows show body region probability maps from the weakly supervised Res U-Net model (where values close to “1” indicate a high probability that voxels belong to one of the body regions), body region masks (obtained by thresholding the probability maps), and manually expert-defined labels, all superimposed on the MIP images. Automated localisation and delineations of all body regions showed excellent agreement with the actual patient anatomy, as demonstrated by a DSC above 0.72 for all three cases when comparing manual and automated masks. Mask for long bones consisted of legs and arms/shoulders.

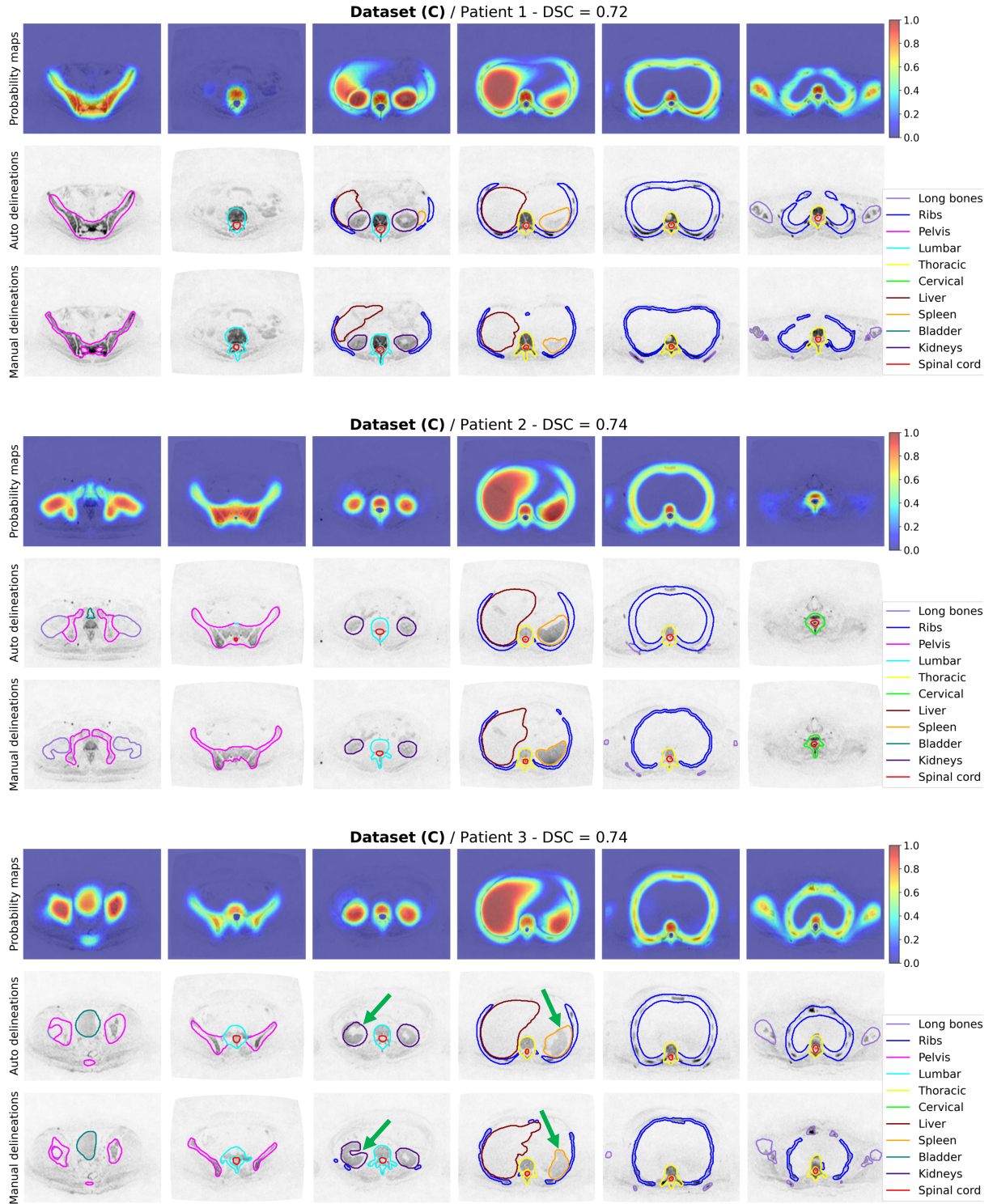


**Figure 5.** Axial b900 images with superimposed manual and automated delineations of the skeleton, adjacent internal organs, and spinal canal for three randomly selected test cases from **Dataset C**. The weakly-supervised Res U-Net model showed high accuracy in localising different anatomical structures, as evidenced by the excellent agreement between the generated probability maps (where values close to “1” indicate a high probability that voxels belong to one of the body regions) and actual patient anatomy. A DSC exceeding 0.72 was obtained for all three cases when comparing manual and automated masks. However, the model might show limitations in precisely capturing the complex details of organ shapes (green arrows). Mask for long bones consisted of legs and arms/shoulders.

### 3.3 Semi-quantitative analysis

In the 15 test patients with APC, the radiologist scored 11 skeleton probability maps as “excellent” and 4 as “good”. For internal organs, 12 probability maps were scored as “excellent” and 3 as “good” (see **Supplementary Material Table 1**). **Figure 6** shows three randomly selected cases. The generated body region probability maps aligned well with the patients’ anatomy, showing no signs of overfitting. Both the skeleton and internal organs were accurately localised within the images, with probabilities exceeding 0.4, while the image background displayed values close to 0, as expected. Importantly, our weakly-supervised Res U-Net model generated reproducible skeletal probability maps in test patients with metastatic bone disease.

In the 15 test patients diagnosed with MM, 10 skeleton probability maps were scored as “excellent” and 5 as “good.” Additionally, 14 probability maps for internal organs were scored as “excellent,” and only 1 as “good” (see **Supplementary Material Table 2**). **Figure 7** presents three randomly selected cases, reinforcing findings from the APC test set. The weakly-supervised Res U-Net consistently generated accurate body region probability maps that closely matched actual patient anatomy, highlighting its potential to automate skeletal delineation from WB-DWI scans in MM patients with active disease.

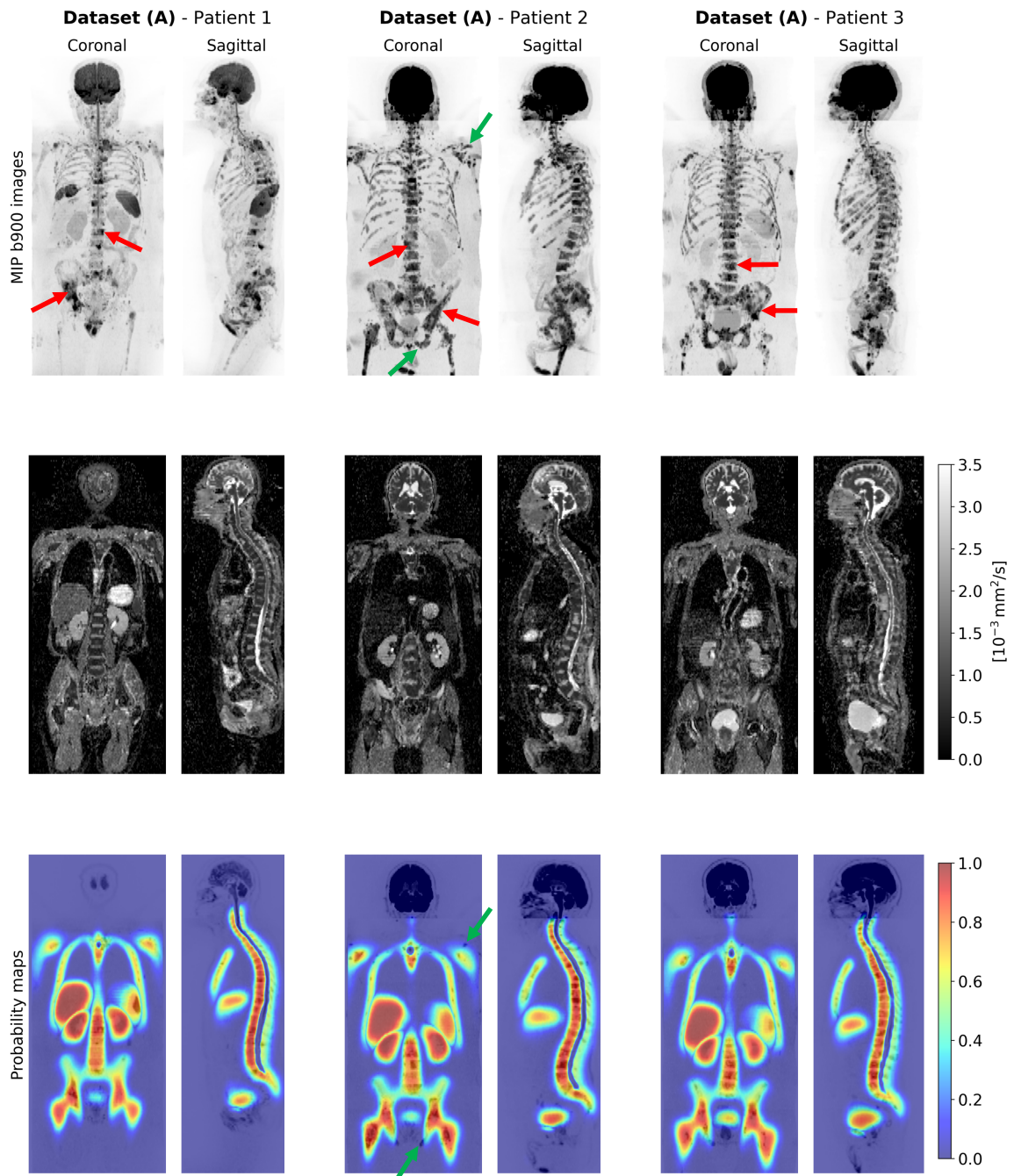


**Figure 6.** Coronal and sagittal views of Maximum Intensity Projection (MIP) of b900 images and ADC maps for three randomly selected APC patients from the test cohort (**Dataset A**) with confirmed diffuse metastatic bone disease. These lesions (red arrows) appear as darker spots with high signal intensity on b900 images and low ADC values (typically  $>5 \cdot 10^{-3} \text{mm}^2/\text{s}$ ) compared to the normal bone marrow background. Superimposed on these MIP images are body region probability maps generated by the weakly-supervised Res U-Net model. The derived probability maps (where values close to “1” indicate a high probability that voxels belong to one of the body regions) accurately matched patient anatomy, ensuring correct positional alignment, volume coverage, and promising boundary delineation between skeletal regions and adjacent internal organs. These findings were supported by expert semi-quantitative analysis, which rated the automated full-body probability maps for these patients as “excellent” (score of 4), except for the skeleton map in “*Patient 2*”, which was rated as “good” (score of 3) due to lower accuracy in localising the top of the shoulders and pubic rami (green arrows).

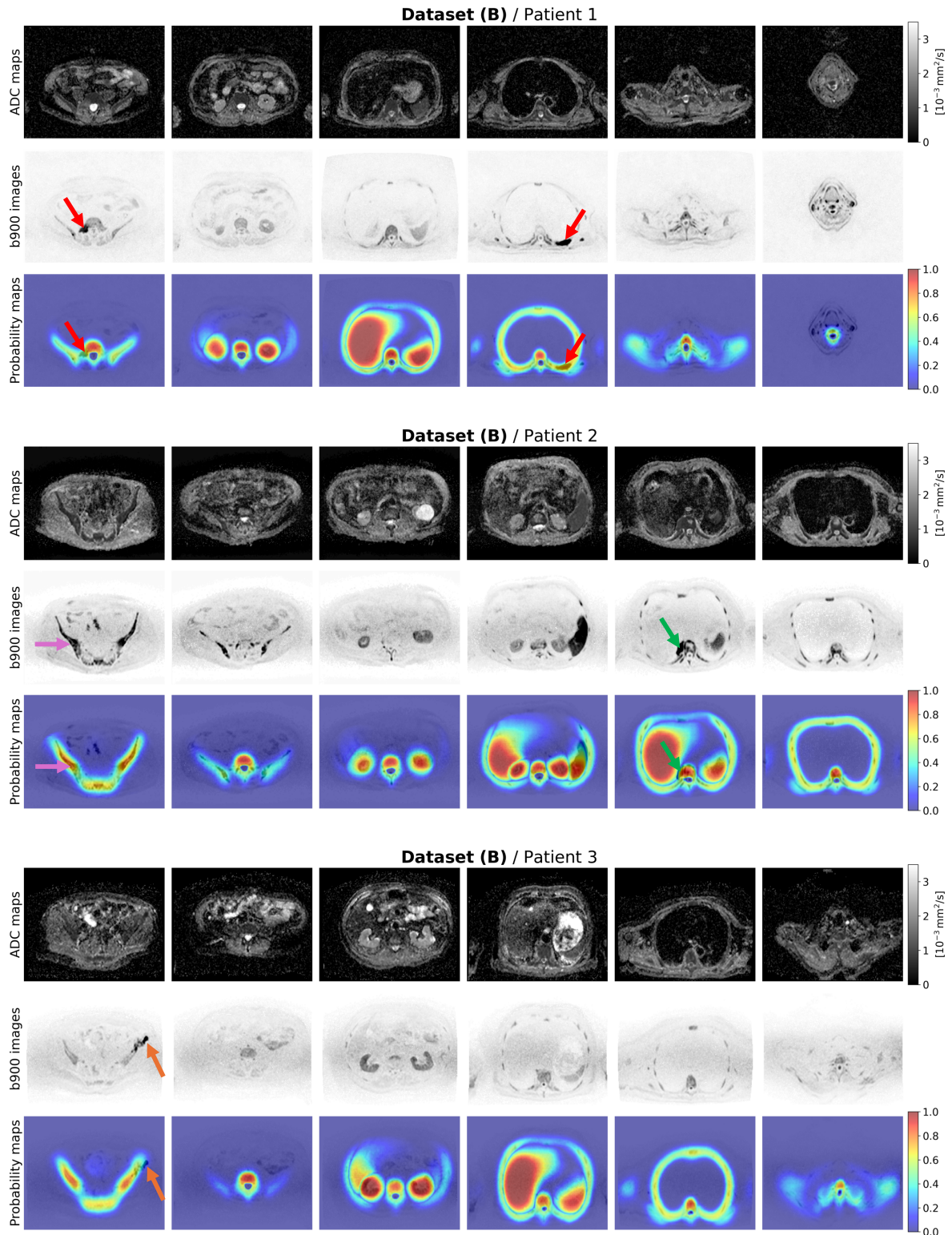


**Figure 7.** Axial ADC maps and b900 images for three patients diagnosed with MM from the test cohort (**Dataset B**), presenting different disease patterns: focal bone lesions (red arrows), diffuse myeloma involvement (purple arrows), and paramedullary disease (green arrows). Body region probability maps derived from the weakly-supervised Res U-Net model were superimposed on the b900 images. These maps demonstrated accurate positional alignment, volume coverage, and clear separation between skeletal regions and adjacent internal organs compared to actual patient anatomy. Expert evaluation rated them as “excellent” (score of 4). However, the skeleton map for “Patient 3” was rated as “good” (score of 3) due to reduced accuracy in delineating the anterior iliac (orange arrows).

## **4. Discussion**

We developed and validated a weakly-supervised deep learning model based on the 3D Res U-Net architecture to automatically localise and delineate seven skeleton regions (legs, pelvis, lumbar/thoracic/cervical spine, ribcage, and arms/shoulders), four internal organs (liver, spleen, urinary bladder, and kidneys), and the spinal canal (spinal cord with surrounding CSF) from WB-DWI scans. We trained a model using an heterogeneous WB-DWI dataset comprising 532 scans from patients with APC or MM, without requiring resources for laborious manual delineations of body regions. Instead, we automated the annotation phase using a validated atlas-based registration algorithm. Manual annotations of body regions can take up to 5-6 hours per WB-DWI scan; however, with our novel methodology, we generated annotations (soft-labels) for 532 scans (~127,500 images) within ~48 hours (~325 seconds/scan).

The quantitative analysis demonstrated that our weakly-supervised Res U-Net model improved accuracy in localising and delineating skeleton and internal organs on test datasets compared to the atlas-based registration algorithm (baseline). For skeleton delineations, we achieved an average DSC, precision, and recall of 0.66/0.6/0.73, respectively. For internal organs, these metrics were 0.79/0.79/0.81, respectively. In contrast to atlas-based registration algorithms, which rely on predefined templates, our deep learning model trained on heterogeneous datasets captures diverse features and patterns, enhancing spatial dependencies and structural information present in WB-DWI scans, thereby leading to improved generalisation on unseen datasets. However, lower performance was observed for ribcage (DSC <0.5) and spleen delineations (average surface distance values exceeding 5mm). This may be due to geometric fidelity issues in the ribcage region from DWI sequence and variability in spleen position between patients due to respiratory motion during free-breathing acquisition [44]. Additionally, training the model using soft-labels might reduce precision in capturing the complex details of organ shapes when compared with manual delineations. Moreover, DWI sequences often suffer from significant geometric distortions and a low SNR, making alignment with anatomical MRI sequences difficult, and further challenging organ delineations. Therefore, our approach of providing



soft-boundaries for delineating skeletal and internal organs may offer a more suitable solution, minimising the risk of fully excluding disease involved areas from the delineated volume.

Spinal canal delineation accuracy was consistent with a previously validated 2D U-Net model, with DSC, precision, and recall above 0.85. Our previous study proven that accurate spinal canal delineations can significantly improve the inter- and intra-patient signal normalisation on WB-DWI [34]. This approach can enhance assessment of bone disease from WB-DWI by improving lesion localisation, diameter measurement, and “at-a-glance” evaluation of post-treatment changes by standardising the display of high-b-value images.

Fast computation and accurate localisation of body region probability maps are key for facilitating clinical deployment of automated tools for disease staging and treatment response assessment. The computational time required to generate probability maps from the weakly-supervised model averaged 25 seconds, compared to the 5 minutes needed for the atlas-based registration algorithm on the same hardware. Furthermore, relative median ADC and volume differences for skeleton segmentations were consistent with an observer repeatability study assessing inter- and intra-reader repeatability of the same biomarkers from manual experts’ delineations of bone lesions in APC patients [45], [46].

To the best of our knowledge, this is the first paper proposing and validating an end-to-end deep learning-based pipeline for automatically localising and delineating body regions from a multi-centre WB-DWI dataset. Standardisation of the WB-DWI protocol is not a trivial task due to the significant number of parameters that can vary across scanners, leading to variability in the quality of the images acquired at different sites, including variations in geometric distortion and SNR [47]. Despite these challenges, our model demonstrated performance comparable to atlas-based registration and deep learning delineations for skeleton and internal organs from high-resolution and high-SNR images previously reported in the literature [19], [28], [48].

Ceranka et al. [19] developed a multi-atlas segmentation algorithm for skeleton delineations from whole-body T1w MRI, reporting a dice score of 0.88 in a LOOCV study with 10 APC patients. However, their method excluded the ribcage and arms/shoulders and required 180 minutes per target image to generate a mask. Lavdas et al. [28] proposed an atlas-based registration algorithm and a convolutional neural network (CNN) to delineate the pelvis, spine, and internal organs (including kidneys, liver, and urinary bladder) from whole-body T2w MRI of 51 volunteers. Their results showed that the CNN outperformed the registration method (dice score 0.81 vs. 0.71). Bauer et al. [48] trained a nnU-Net on 210 coronal T1w MRI scans to delineate the spine, pelvis, humeri, and femora, achieving a dice score of 0.88 in 21 test patients with myeloma-related pathologies. However, their approach relied on T1w coronal MRI, which is not included in the MY-RADS guidelines for myeloma assessment and required 18 minutes per scan to generate a mask.

To directly benchmark our model, we evaluated it against the open-source *TotalSegmentator-MRI* nnU-Net model (ver. 2.7.0) [49] using whole-body  $b = 50$  s/mm<sup>2</sup> images (which best matched the open-source model's training datasets) from the atlas cohort (15 MM patients). Our weakly-supervised ResU-Net model outperformed *TotalSegmentator-MRI* for skeleton delineation (excluding the ribcage, which *TotalSegmentator-MRI* does not segment), achieving a dice score of 0.73 vs. 0.68 ( $p < 0.05$ , paired t-test), with a relative error in delineated skeleton volumes of +6% vs. -35%. The largest score difference was observed for the spine (0.78 vs. 0.58,  $p < 0.05$ ), while spinal canal delineation showed no significant difference (0.84 vs. 0.82). Moreover, *TotalSegmentator-MRI* achieved higher accuracy for internal organ delineation (dice score of 0.8 vs. 0.87,  $p < 0.05$ ), with the spleen showing the highest score difference between models (0.66 vs. 0.8,  $p < 0.05$ ). Nevertheless, these findings are encouraging, considering the advantages of our calibrated deep-learning model: (i) it is designed to generate soft-boundary maps, improving the delineation of anatomical structures with unclear boundaries due to disease spread, as well as the low resolution and geometric distortion of DWI; (ii) it generates delineations in 25 seconds per WB-DWI scan, compared to 12 minutes for the open-source model, with both tested on a CPU (Apple M3 Max, 16-core). This reduces dependence on dedicated GPUs, which are less available in hospitals for on-premises AI model deployment.

A limitation of the developed weakly-supervised Res U-Net model is that the training data were obtained from a single MRI vendor. However, the automated annotation phase could aid in the model's re-training or application of transfer learning techniques. This would involve using WB-DWI scans acquired from different scanner manufacturers and/or leveraging novel AI-based reconstruction methods [50]. Such strategies aim to enhance the model's ability to generalise to unseen data without the need for manual delineation of skeleton regions and internal organs.

We acknowledge the limitation of testing the weakly-supervised deep learning model solely using the atlas dataset. While our findings could be further validated with manual contours from larger external WB-DWI datasets, we have provided supplementary evidence of the model's accuracy in localising and delineating body regions from WB-DWI scans included in an independent test dataset with 15 APC patients and 15 patients with confirmed MM. Our semi-quantitative analysis indicated no evidence of overfitting with probability maps for the skeleton and internal organs showing remarkable agreement with actual patient anatomy as confirmed by the radiologist's assessment. The results showed 47 body region probability maps scored as "excellent" and only 13 rated as "good." These findings demonstrate the potential of the weakly-supervised deep-learning model as preliminary step for developing WB-DWI signal-based AI tools for detecting/delineating suspected malignant bone lesions [51]. This two-step approach enables the automatic quantification of disease burden and the measurement of ADC statistics and TDV from WB-DWI scans of patients who may present significant disease burden, multifocal lesions or paramedullary disease. When applied to both pre- and post-treatment scans, it enables the tracking of changes in ADC and TDV, reflecting treatment-induced effects on bone marrow space. This information could support radiologists and clinicians in developing personalised treatment strategies, ultimately improving patient outcomes.

General observations provided by the radiologist included: (i) excellent segmentations of the spinal canal; (ii) a tendency to under-segment the inferior pubic rami, but no false positives from including pelvic organs/vessels; (iii) no false positives from thigh vessels; (iv) no false positives from axillary lymph nodes. This latter point is extremely encouraging, considering we have not delineated lymph

nodes as part of this product development. While these structures can be in close proximity to skeletal structures (e.g. axillary nodes to ribs, retroperitoneal nodes to spine, pelvic side wall nodes to pelvic bones etc), the distribution, morphology and size of lymph nodes can be extremely variable even within the realm of normal anatomy, making the segmentation process impractical due to resources limitations at this time.

In conclusion, our novel weakly-supervised deep learning model, based on the 3D Res U-Net architecture, can swiftly generate accurate and reproducible probability maps for localising skeletal regions, internal organs, and the spinal canal from WB-DWI scans. This will facilitate the development of automated tools for delineating suspected bone disease, based on WB-DWI signal intensity. This in turn could enable the extraction of quantitative imaging biomarkers for staging and treatment response assessment. Prospective evaluation of our tool in a multi-centre setting is currently ongoing, as part of a national trial assessing the effectiveness of these tools for automatically delineating metastatic bone disease or multifocal myeloma lesions from WB-DWI in patients with APC and MM.

**Supplementary Material Table 1.** Semi-quantitative analysis of derived skeleton and internal organ probability maps from the semi-supervised deep learning model, evaluated by an experienced radiologist using scans acquired from patients with metastatic bone disease (test cohort, **Dataset A**). Probability maps were rated on a 4-point Likert scale: 1 = failed, 2 = suboptimal, 3 = good, 4 = excellent.

APC test cohort (Dataset A)	Skeletal probability map	Internal organ probability map	Overall score	Radiologist comments
001	4	4	4	
002	4	4	4	
003	4	4	4	
004	3	3	3	Part of the spleen included in the ribcage. Also top of the shoulders not included in skeleton. A part of a retroperitoneal lymph nodes included under low probability spine
005	3	4	4	Top of the left shoulder not included in skeleton
006	4	3	4	Part of spleen included under ribcage
007	4	4	4	
008	4	4	4	
009	4	4	4	
010	4	4	4	Very good negotiation between retroperitoneal lymph nodes and spine, and between spleen and ribcage
011	3	4	4	Tops of shoulder, inferior pubic rami, and right pubic bone disease under very low probability, [however high volume of disease so these minor areas are not significant]
012	3	3	3	Part of the spleen included in the ribcage. Also top of the shoulders not included in skeleton
013	4	4	4	
014	4	4	4	
015	4	4	4	

**Supplementary Material Table 2.** Semi-quantitative analysis of derived skeleton and internal organ probability maps from the semi-supervised deep learning model, evaluated by an experienced radiologist using scans acquired from MM patients (test cohort, **Dataset B**). Probability maps were scored on a 4-point Likert scale: 1 = failed, 2 = suboptimal, 3 = good, 4 = excellent.

MM test cohort (Dataset B)	Skeleton probability map	Internal organ probability map	Overall score	Radiologist comments
001	4	4	4	
002	4	4	4	
003	4	4	4	
004	4	4	4	
005	3	4	4	Missed inferior pubic rami, top of acromioclavicular joints, and distal right femur
006	4	3	4	right kidney partially included in liver
007	4	4	4	Very difficult scan. Excellent negotiation of large artefacts from breast implants
008	4	4	4	Some tips of transverse processes and very lateral end of right clavicle under very low probability, [however, in the face of such high-volume disease these are insignificant]
009	4	4	4	
010	4	4	4	Excellent demarcation between artefact and right 1 <sup>st</sup> rib
011	3	4	4	Very top of the shoulders under very low probability
012	3	4	4	Post edge of paramedullary disease sternum on the very low probability values - 0.05
013	3	4	4	Part of paramedullary disease head of lower right rib on low probability values - 0.2
014	4	4	4	Two lesions top of shoulders - included!
015	3	4	4	Part of left anterior iliac lesion under very low probability. Same with left lateral and bilateral mid clavicles

- **Author Contributions**

Conceptualization, A.C., M.D.B. and D.-M.K.; methodology, A.C. and M.D.B.; software, A.C. and R.H.; validation, A.C., R.H., M.D.B., N.T., C.M., A.D. and D.-M.K.; formal analysis, A.C.; resources, R.D., C.M. and N.T.; data curation, A.C. and R.H.; writing-original draft preparation, A.C.; writing-review and editing, A.C., R.H., A.R., R.D., A.D., C.M., N.T., M.D.B. and D.-M.K.; supervision, M.D.B. and D.-M.K.; project administration, A.R.; funding acquisition, M.D.B. and D.-M.K. All authors have read and agreed to the published version of the manuscript.

- **Funding**

This project is funded by the NIHR Invention for Innovation award (Advanced computer diagnostics for whole body magnetic resonance imaging to improve management of patients with metastatic bone cancer II-LA-0216-20007).

- **Informed Consent Statement**

Patient consent was waived; study was conducted with retrospective data only and researchers only had access to de-identified data.

- **Data Availability Statement**

Data can be shared upon request from the authors. However, this is subject to the establishment of an appropriate data-sharing agreement, given the sensitive nature of patient information involved.

- **Acknowledgments**

This study represents independent research funded by the National Institute for Health and Care Research (NIHR) Biomedical Research Centre at The Royal Marsden NHS Foundation Trust and The Institute of Cancer Research, London, and by the Royal Marsden Cancer Charity and Cancer Research UK (CRUK) National Cancer Imaging Trials Accelerator (NCITA), and is funded by the NIHR Invention for Innovation award (Advanced computer diagnostics for whole body magnetic resonance imaging to improve management of patients with metastatic bone cancer II-LA-0216-20007). The views expressed are those of the author(s) and not necessarily those of the NIHR or the Department of Health and Social Care. This work uses data provided by patients and collected by the NHS as part of their care and support.

The authors would also like to acknowledge Mint Medical®.

- **Conflicts of interest**

A.C., R.H., and M.D.B. have submitted a patent to the UK Intellectual Property Office regarding the work described in this manuscript.

## References

- [1] A. R. Padhani *et al.*, “Rationale for Modernising Imaging in Advanced Prostate Cancer,” *Eur Urol Focus*, vol. 3, no. 2–3, pp. 223–239, 2017
- [2] C. Messiou *et al.*, “Prospective Evaluation of Whole-Body MRI versus FDG PET/CT for Lesion Detection in Participants with Myeloma,” *Radiol Imaging Cancer*, vol. 3, no. 5, 2021
- [3] N. Tunariu *et al.*, “What’s New for Clinical Whole-body MRI (WB-MRI) in the 21st Century,” *Br J Radiol*, vol. 93, pp. 1–13, 2020
- [4] D. M. Koh *et al.*, “Whole-body diffusion-weighted mri: Tips, tricks, and pitfalls,” *American Journal of Roentgenology*, vol. 199, no. 2, pp. 252–262, 2012
- [5] R. Perez-lopez, D. N. Rodrigues, I. Figueiredo, J. Mateo, and D. J. Collins, “Multiparametric Magnetic Resonance Imaging of Prostate Cancer Bone Disease Correlation with Bone Biopsy Histological and Molecular Features,” *Invest Radiol*, vol. 53, no. 2, 2018
- [6] A. R. Padhani, K. Van Ree, D. J. Collins, S. D’Sa, and A. Makris, “Assessing the relation between bone marrow signal intensity and apparent diffusion coefficient in diffusion-weighted MRI,” *American Journal of Roentgenology*, vol. 200, no. 1, pp. 163–170, 2013
- [7] A. R. Padhani and A. Gogbashian, “Bony metastases: Assessing response to therapy with whole-body diffusion MRI,” *Cancer Imaging*, vol. 11, 2011
- [8] M. Wennmann *et al.*, “Repeatability and Reproducibility of ADC Measurements and MRI Signal Intensity Measurements of Bone Marrow in Monoclonal Plasma Cell Disorders: A Prospective Bi-institutional Multiscanner, Multiprotocol Study,” *Invest Radiol*, vol. 57, no. 4, pp. 272–281, 2022
- [9] R. Perez-Lopez *et al.*, “Volume of bone metastasis assessed with whole-Body Diffusion-weighted imaging is associated with overall survival in metastatic castration resistant prostate cancer,” *Radiology*, vol. 280, no. 1, pp. 151–160, 2016
- [10] R. Perez-Lopez *et al.*, “Diffusion-weighted imaging as a treatment response biomarker for evaluating bone metastases in prostate cancer: A pilot study,” *Radiology*, vol. 283, no. 1, pp. 168–177, 2017
- [11] A. R. Padhani *et al.*, “METastasis Reporting and Data System for Prostate Cancer: Practical Guidelines for Acquisition, Interpretation, and Reporting of Whole-body Magnetic Resonance Imaging-based Evaluations of Multiorgan Involvement in Advanced Prostate Cancer,” *Eur Urol*, vol. 71, no. 1, pp. 81–92, 2017
- [12] C. Messiou *et al.*, “Guidelines for Acquisition, Interpretation, and Reporting of Whole-Body MRI in Myeloma: Myeloma Response Assessment and Diagnosis System (MY-RADS),” *Radiology*, vol. 291.1, no. 7, 2019
- [13] M. D. Blackledge *et al.*, “Assessment of treatment response by total tumor volume and global apparent diffusion coefficient using diffusion-weighted MRI in patients with metastatic bone disease: A feasibility study,” *PLoS One*, vol. 9, no. 4, pp. 1–8, 2014
- [14] A. R. Padhani, D. M. Koh, and D. J. Collins, “Whole-body diffusion-weighted MR imaging in cancer: Current status and research directions,” *Radiology*, vol. 261, no. 3, pp. 700–718, 2011
- [15] Y. Gao *et al.*, “Treatment Response Assessment in Multiple Myeloma: Histogram Analysis of Total Tumor Apparent Diffusion Coefficient based on Whole-body Diffusion-weighted MR Imaging,” *Journal of Magnetic Resonance Imaging*, vol. 60, no. 3, pp. 1051–1060, 2024
- [16] Q. Wang *et al.*, “Histogram Analysis Based on Apparent Diffusion Coefficient Maps of Bone Marrow in Multiple Myeloma: An Independent Predictor for High-risk Patients Classified by the Revised International Staging System,” *Acad Radiol*, vol. 29, no. 6, pp. e98–e107, 2022
- [17] S. D. Almeida *et al.*, “Quantification of tumor burden in multiple myeloma by atlas-based semi-automatic segmentation of WB-DWI,” *Cancer Imaging*, vol. 20, no. 1, pp. 1–10, 2020



- [18] H. Arabi and H. Zaidi, “Comparison of atlas-based techniques for whole-body bone segmentation,” *Med Image Anal*, vol. 36, pp. 98–112, 2017
- [19] J. Ceranka *et al.*, “Multi-atlas segmentation of the skeleton from whole-body MRI—Impact of iterative background masking,” *Magn Reson Med*, vol. 83, no. 5, pp. 1851–1862, 2019
- [20] M. Cabezas, A. Oliver, X. Lladó, J. Freixenet, and M. Bach Cuadra, “A review of atlas-based segmentation for magnetic resonance brain images,” *Comput Methods Programs Biomed*, vol. 104, no. 3, pp. 158–177, 2011
- [21] J. E. Iglesias and M. R. Sabuncu, “Multi-Atlas Segmentation of Biomedical Images: A Survey,” *Med Image Anal.*, vol. 24, no. 1, pp. 205–219, 2015
- [22] Y. Lei *et al.*, “Deep Learning in Multi-organ Segmentation,” 2020 [Online]. Available: <https://arxiv.org/abs/2001.10619>
- [23] T. Vrtovec, D. Močnik, P. Strojjan, F. Pernuš, and B. Ibragimov, “Auto-segmentation of organs at risk for head and neck radiotherapy planning: From atlas-based to deep learning methods,” *Med Phys*, vol. 47, no. 9, pp. e929–e950, 2020
- [24] W. Chi, L. Ma, J. Wu, M. Chen, W. Lu, and X. Gu, “Deep learning-based medical image segmentation with limited labels,” *Phys Med Biol*, vol. 65, no. 23, p. 235001, 2020
- [25] Y. Liu *et al.*, “Genetic architecture of 11 organ traits derived from abdominal MRI using deep learning,” *Elife*, vol. 10, 2021
- [26] N. Bastý, Y. Liu, M. Cule, E. L. Thomas, J. D. Bell, and B. Whitcher, “Automated Measurement of Pancreatic Fat and Iron Concentration Using Multi-Echo and T1-Weighted MRI Data,” *Proceedings - International Symposium on Biomedical Imaging*, pp. 345–348, 2020
- [27] Y. Deng *et al.*, “An effective U-Net and BiSeNet complementary network for spine segmentation,” *Biomed Signal Process Control*, vol. 89, 2024
- [28] I. Lavdas *et al.*, “Fully automatic, multiorgan segmentation in normal whole body magnetic resonance imaging (MRI), using classification forests (CFS), convolutional neural networks (CNNs), and a multi-atlas (MA) approach,” *Med Phys*, vol. 44, no. 10, pp. 5210–5220, 2017
- [29] X. Liu *et al.*, “Fully automated pelvic bone segmentation in multiparametric MRI using a 3D convolutional neural network,” *Insights Imaging*, vol. 12, no. 1, 2021
- [30] J. Wasserthal *et al.*, “TotalSegmentator: Robust Segmentation of 104 Anatomic Structures in CT Images,” *Radiol Artif Intell*, vol. 5, no. 5, 2023
- [31] C. Sun, A. Shrivastava, S. Singh, and A. Gupta, “Revisiting Unreasonable Effectiveness of Data in Deep Learning Era.” 2017 [Online]. Available: <https://arxiv.org/abs/1707.02968>
- [32] M. Rata *et al.*, “Implementation of Whole-Body MRI (MY-RADS) within the OPTIMUM/MUKnine multi-centre clinical trial for patients with myeloma,” *Insights Imaging*, vol. 13, no. 1, pp. 1–16, 2022
- [33] A. Candito *et al.*, “Deep learning assisted atlas-based delineation of the skeleton from Whole-Body Diffusion Weighted MRI in patients with malignant bone disease,” *Biomed Signal Process Control*, vol. 92, 2024
- [34] A. Candito *et al.*, “Deep Learning for Delineation of the Spinal Canal in Whole-Body Diffusion-Weighted Imaging: Normalising Inter- and Intra-Patient Intensity Signal in Multi-Centre Datasets,” *Bioengineering*, vol. 11, no. 2, p. 130, 2024
- [35] J. P. Thirion, “Image matching as a diffusion process: An analogy with Maxwell’s demons,” *Med Image Anal*, vol. 2, no. 3, pp. 243–260, 1998
- [36] E. Kerfoot, J. Clough, I. Oksuz, J. Lee, A. P. King, and J. A. Schnabel, “Left-Ventricle Quantification Using Residual U-Net,” *Lecture Notes in Computer Science (including subseries Lecture Notes in Artificial Intelligence and Lecture Notes in Bioinformatics)*, vol. 11395 LNCS, pp. 371–380, 2019

- [37] M. D. Blackledge *et al.*, “Computed Diffusion-weighted MR Imaging May Improve Tumor Detection,” *Radiology*, vol. 261, no. 2, pp. 573–81, 2011
- [38] M. D. Blackledge *et al.*, “Noise-Corrected, Exponentially Weighted, Diffusion-Weighted MRI (niceDWI) Improves Image Signal Uniformity in Whole-Body Imaging of Metastatic Prostate Cancer,” *Front Oncol*, vol. 10, pp. 1–12, 2020
- [39] Q. Jia and H. Shu, “BiTr-UNet: a CNN-Transformer Combined Network for MRI Brain Tumor Segmentation,” 2021 [Online]. Available: <https://arxiv.org/abs/2109.12271>
- [40] C. F. Dormann, “Calibration of probability predictions from machine-learning and statistical models,” *Global Ecology and Biogeography*, vol. 29, no. 4, pp. 760–765, 2020
- [41] F. M. Ojeda *et al.*, “Calibrating machine learning approaches for probability estimation: A comprehensive comparison,” *Stat Med*, vol. 42, no. 29, pp. 5451–5478, 2023
- [42] R. Caruana, “Predicting Good Probabilities with Supervised Learning,” *Proceedings of the 22nd international conference on Machine learning*, 2005
- [43] U. Johansson, H. Boström, L. Carlsson, Z. Luo, G. Cherubin, and K. A. Nguyen, “Calibrating Multi-Class Models,” *Proc Mach Learn Res*, vol. 152, pp. 1–20, 2021
- [44] S. Keaveney *et al.*, “Image quality in whole-body MRI using the MY-RADS protocol in a prospective multi-centre multiple myeloma study,” *Insights Imaging*, vol. 14, no. 1, pp. 1–14, 2023
- [45] R. Donners *et al.*, “Repeatability of quantitative individual lesion and total disease multiparametric whole-body MRI measurements in prostate cancer bone metastases,” *British Journal of Radiology*, vol. 96, no. 1151, 2023
- [46] M. D. Blackledge *et al.*, “Inter- and Intra-Observer Repeatability of Quantitative Whole-Body, Diffusion-Weighted Imaging (WBDWI) in Metastatic Bone Disease,” *PLoS One*, vol. 11, no. 4, pp. 1–12, 2016
- [47] A. Barnes *et al.*, “Guidelines & recommendations: UK quantitative WB-DWI technical workgroup: Consensus meeting recommendations on optimisation, quality control, processing and analysis of quantitative whole-body diffusion-weighted imaging for cancer,” *British Journal of Radiology*, vol. 91, no. 1081, pp. 1–12, 2018
- [48] F. Bauer *et al.*, “Advanced Automated Model for Robust Bone Marrow Segmentation in Whole-body MRI,” *Acad Radiol*, 2025
- [49] T. Akinci D’Antonoli *et al.*, “TotalSegmentator MRI: Robust Sequence-independent Segmentation of Multiple Anatomic Structures in MRI,” *Radiology*, vol. 314, no. 2, p. e241613, 2025
- [50] K. Zormpas-Petridis *et al.*, “Accelerating whole-body diffusion-weighted mri with deep learning-based denoising image filters,” *Radiol Artif Intell*, vol. 3, no. 5, 2021
- [51] A. Candito, M. D. Blackledge, R. Holbrey, and D.-M. Koh, “Automated tool to quantitatively assess bone disease on Whole-Body Diffusion Weighted Imaging for patients with Advanced Prostate Cancer,” *Medical Imaging with Deep Learning (MIDL)*, 2022